Quantum-Monte-Carlo studies of superconductivity in strongly correlated systems

Autor(en):   **Dopf, G. / Wagner, J. / Dieterich, P.**

QUANTUM-MONTE-CARLO STUDIES OF SUPERCONDUCTIVITY IN STRONGLY CORRELATED SYSTEMS

G. Dopf, J. Wagner, P. Dieterich, A. Muramatsu, and W. Hanke

Physikalisches Institut, Universität Würzburg, Am Hubland,

D-8700 Würzburg, Federal Republic of Germany

Quantum-Monte-Carlo (QMC) simulations are reviewed, which aim at a quantitative understanding of the multi-orbital 2-D Hubbard model, as it relates to the unusual properties of the normal state of the high-T_c cuprates and possibly to the microscopic nature of the superconducting pairing. In a first step, by comparing QMC results with experimental data on electronic and magnetic excitations, a unique parameter set is determined which clearly (also for dopings $x \neq 0$) places the high-T_c cuprates in the strongly correlated regime. A new dynamical extension of the QMC technique reveals that the states near E_F are related to the Zhang-Rice $Cu - O$ singlet construction. They are found to have a band-like dispersion with also Fermi velocity and location in close accord with photoemission data. Whereas the imaginary part of the self-energy displays non-Fermi liquid behavior for smaller dopings ($x \cong 0.25$), for larger dopings ($x \cong 0.5$) the Fermi liquid picture is restored. Besides the normal state properties we also extract superconducting pair-field susceptibilities for various symmetry channels. As a particularly noteworthy result, we find the interaction vertex in the extended s-channel to show a maximum for $x \sim 0.2$, closely resembling the experimental dependence of T_c on doping.

I.   Introduction

A considerable effort was invested in recent years towards a determination of the relevant parameter region for different models for high temperature superconductors (HTS). Among the most popular ones, the three-band Hubbard model is closest to the real systems. Several groups proposed sets of parameters that were derived using different approximation schemes like constrained local density calculations[1] together with a mean-field treatment[2], the Anderson impurity model[3] complemented with experimental spectroscopic data[4], cluster calculations[5, 6], Lanczos exact diagonalization for small clusters[7]. It would be highly desirable however to test such parameters with a method that on the one hand goes beyond the mean-field approximation, since electronic correlation is one of the central new features in these materials, and on the other hand, is not limited to only small clusters but is capable of extrapolating information relevant to the thermodynamic limit. It would be also extremely important to be able to make a direct comparison with different experimental results, where the dependence on doping remains one of the most salient features in the HTS, since not only T_c shows a pronounced dependence[8] but also normal state properties like the magnetic susceptibility[9], Hall effect[10] and thermopower[11] show a characteristic behavior on doping. Such a comparison was recently done by Trugman[12], but again a variational method was used, and several assumptions like a rigid band based on the properties of one hole bring uncertainties upon

the relevance of the results. Moreover a crucial point, namely superconducting properties, are almost not referred to in the above mentioned theoretical works.

In order to make the paper self contained we describe the essential features of the often discussed one-band Hubbard model. After that we present a detailed study of the more complicated three-band Hubbard model, where a determination of the relevant parameter set leads to a close agreement with experiments on high-T_c materials for the following normal state-properties in a) the undoped phase: charge-transfer gap, antiferromagnetic long-range order and in b) the doped phase: magnetic susceptibility, incommensurate spin structure, one-particle spectrum. In particular the study of the one-particle spectrum complemented with exact diagonalization studies for the lifetime of the states close to the Fermi surface gives strong indication that the normal state properties are better described as a Luttinger liquid instead of a Fermi liquid. This finding has profound implications for the superconducting state since until now the theoretical understanding of superconductivity is based on the existence of a Fermi liquid in the normal state. As for the superconducting properties we find that the interaction vertex for the pairing correlation function in the extended s-channel shows a maximum for $\delta \sim 20\%$, closely resembling the dependence of T_c on doping. This feature is not present for other symmetries of the order parameter or in other parameter regions.

The paper is organized as follows: In chapter 2 we give a short introduction into the one-band model and

we describe the simulated three-band model and the used Quantum-Monte-Carlo algorithms. The next chapter presents results for magnetic properties of the model, namely the structure form factor and the magnetic susceptibility. We analyze both quantities in the undoped as well as in the doped case. Moreover we discuss the low-lying single-particle excitations in the three-band model and compare our results directly with angle resolved photoemission and inverse photoemission results. Chapter 4 deals with the question of superconductivity in the model. We analyze the interaction vertex as a function of doping and discuss the effects of temperature on our present results. Chapter 5 gives the conclusion.

II.   Hamilton Operators and Algorithms

A.   One-band Hubbard Model

The most popular model to study the strongly correlated electrons is the one-band Hubbard model, which is given through

$$H = -t \sum_{<ij>} (c_{i\sigma}^{\dagger} c_{j\sigma} + h.c.) + U \sum_{i} n_{i\uparrow} n_{i\downarrow}. \quad (2.1)$$

This model describes fermions on a square lattice, where the operator $c_{i\sigma}^{\dagger}$ ($c_{i\sigma}$) creates (annihilates) a fermion at site i with spin σ. $n_{i\sigma} = c_{i\sigma}^{\dagger} c_{i\sigma}$ gives the occupation number operator. The symbol $<ij>$ stands for a sum over all nearest neighbors of a site i. t is the hopping-matrix element between the sites on the lattice. The first part of the Hamiltonian describes the kinetic processes in the model. U is the Hubbard interaction, which describes a local Coulomb-repulsion and is responsible for the correlation effects in the system. The bandwidth is given through $W = 8t$. Concerning the experimental situation in the high-T_c-materials, the one-band model describes only the copper sublattice. The knowledge about the Hubbard model is mainly based on the results of exact numerical techniques. We want to summarize here the basic features, which emerged from Quantum-Monte-Carlo simulations.

In the undoped phase the ground state has long-range antiferromagnetic order[13, 14] for a wide range of interaction strengths U. The antiferromagnetic order is rapidly suppressed, if the system is doped away from half-filling. This fact is reflected in the magnetic structure factor. In the undoped case the magnetic structure factor results in a peak at (π, π), which shifts out along the $(\pi, \pi - \Delta q)$ and $(\pi - \Delta q, \pi)$ edges and becomes significantly weaker[15]. However, there
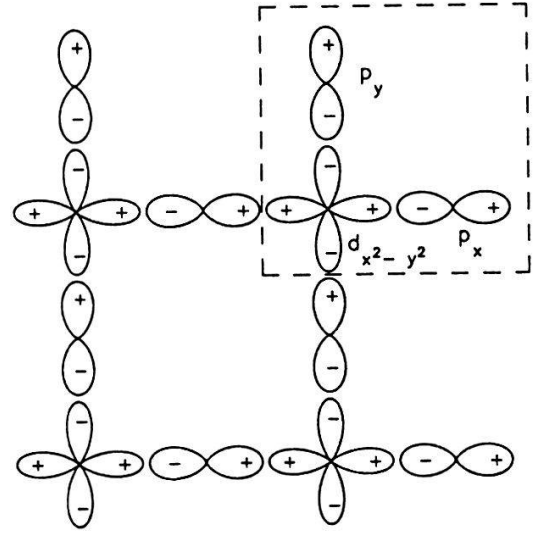

Figure 1: Schematic representation of Cu-$3d_{x^2-y^2}$- and O-$2p_x$- or $2p_y$-orbitals.

is no evidence of long-range incommensurate order near half-filling.

Concerning the superconducting properties one finds attractive interaction between two fully dressed one-particle excitations in the d-wave channel[16]. However, the extrapolation to the thermodynamic limit shows no long range superconducting order.

B.   Three-band Hubbard Model

The Hamiltonian for the CuO_2-planes is defined by:

$$H = \sum_{\substack{i,j \\ \sigma}} \varepsilon_{ij} c_{i\sigma}^{\dagger} c_{j\sigma} + \frac{1}{2} \sum_{\substack{i,j \\ \sigma\sigma'}} U_{ij} n_{i\sigma} n_{j\sigma'}, \quad (2.2)$$

where $c_{i\sigma}^{\dagger}$ creates a hole in the Cu-$3d_{x^2-y^2}$- and in the O-$2p_x$- or $2p_y$-orbital depending on the site i. A schematic representation of the orbitals is given in Figure 1. ε_{ij} includes the on-site energies ε_d (Cu) and ε_p (O) with $\Delta = \varepsilon_p - \varepsilon_d$ and a Cu-O hopping t_{Cu-O} (O-O hopping t_{O-O}), while U_{ij} describes the on-site Coulomb energies U_d and U_p and the inter-site Cu-O interaction U_{pd}.

Now we give a short description of the algorithm used to perform finite temperature studies of a grand canonical ensemble. The basic developments are due to Blankenbecler, Scalapino and Sugar[18] (BSS), and to Hirsch[19], who applied the algorithm for the first time to the Hubbard model. Further improvements, that allow for low temperature simulations were achieved very recently[13].

Our aim is to calculate the expectation value of a

physical observable $\mathcal{O}$, defined by

$$< \mathcal{O} > = \frac{Tr(\mathcal{O}e^{-\beta H})}{Tr(e^{-\beta H})}. \qquad (2.3)$$

To this end a small imaginary time step $\Delta\tau$ ($\beta = L\Delta\tau$) is introduced and by means of the Trotter formula the partition function can be written in the following form

$$\begin{aligned} Z &= Tr(e^{-\beta H}) \\ &= Tr(e^{-\Delta\tau K_1}e^{-\Delta\tau K_2}e^{-\Delta\tau V_d}e^{-\Delta\tau V_p}e^{-\Delta\tau V_{pd}})^L \\ &\quad + O((\Delta\tau)^2). \end{aligned} \qquad (2.4)$$

The first exponent corresponds to the p-d hybridization,

$$\begin{aligned} K_1 &= \sum_{<i,j>\,\sigma} t_{ij}(d_{i,\sigma}^\dagger c_{j,\sigma} + h.c.) \\ &= \sum_{<i,j>\,\sigma} d_{i,\sigma}^\dagger k_{i,j}^{(1)} c_{j,\sigma}, \end{aligned} \qquad (2.5)$$

and the second one is due to the direct O-O hopping

$$\begin{aligned} K_2 &= \sum_{<j,j'>\,\sigma} \bar{t}_{jj'}(c_{j,\sigma}^\dagger c_{j',\sigma} + h.c.) \\ &= \sum_{<j,j'>\,\sigma} c_{j,\sigma}^\dagger k_{j,j'}^{(2)} c_{j',\sigma}. \end{aligned} \qquad (2.6)$$

The other terms refer to the potential and interaction parts both on Cu- and O-sites.

$$V_\alpha = U_\alpha \sum_m n_{m,\uparrow}^\alpha n_{m,\downarrow}^\alpha + (\epsilon_\alpha - \mu) \sum_{m,\sigma} n_{m,\sigma}^\alpha, \qquad (2.7)$$

$$V_{pd} = U_{pd} \sum_{\substack{<i,j>\\ \sigma\sigma'}} n_{i,\sigma}^d n_{j,\sigma'}^p, \qquad (2.8)$$

where α corresponds to d or p depending on whether m is a Cu- or an O-site.

A discrete Hubbard-Stratonovich transformation is applied to the interaction terms, in order to bring them into a bilinear form[20],

$$\begin{aligned} &\exp(-\Delta\tau U_\alpha n_{m,\uparrow}^\alpha n_{m,\downarrow}^\alpha) \\ &= \frac{1}{2}Tr_{\sigma_{m,l}} \exp[\lambda_\alpha \sigma_{m,l}(n_{m,\uparrow}^\alpha - n_{m,\downarrow}^\alpha) - \\ &\quad -\frac{1}{2}U_\alpha \Delta\tau(n_{m,\uparrow}^\alpha + n_{m,\downarrow}^\alpha)], \end{aligned} \qquad (2.9)$$

with

$$\tanh^2\left(\frac{\lambda_\alpha}{2}\right) = \tanh\left(\frac{\Delta\tau U_\alpha}{4}\right). \qquad (2.10)$$

A similar transformation is used for the operators corresponding to U_{pd}. The Hubbard-Stratonovich transformation must be performed on each lattice site m

and at each time slice l, therefore the auxiliary Ising variable $\sigma_{m,l}$ has the corresponding two space-time indices. Since the original Hamiltonian was mapped into a free Fermion system interacting with a fluctuating classical field, the quantum mechanical trace can be now performed. The result is

$$Z = \sum_{\{\sigma_{m,l}\}} (detO^+ detO^-), \qquad (2.11)$$

with

$$O^\pm = I + B_L^\pm B_{L-1}^\pm \dots B_1^\pm \qquad (2.12)$$

and

$$B_l^\pm = e^{-\Delta\tau k^{(1)}} e^{-\Delta\tau k^{(2)}} e^{v_1^\pm(l)} e^{v_2^\pm(l)}. \qquad (2.13)$$

In the last line we denoted

$$v_\alpha^\pm(l) = \delta_{m,m'}\left(\pm\lambda_\alpha \sigma_{m,l} + \Delta\tau\left(\mu - \epsilon_\alpha - \frac{U_\alpha}{2}\right)\right) \qquad (2.14)$$

The Fermion determinants $detO^\pm$ are functionals of the Ising-field $\sigma_{m,l}$.

A sequence of Hubbard Stratonovich fields $\{\sigma_{m,l}\}$ is generated, which are distributed according to $|detO^+ detO^-|/Z$ using a standard Monte Carlo method. We reject or accept a spin flip in the 3-D Ising lattice according to a heat-bath algorithm[21]. The probability for acceptance is

$$P = \frac{R^+ R^-}{1 + R^+ R^-}, \qquad (2.15)$$

with

$$R^\pm = \frac{|(detO^\pm)_{new}|}{|(detO^\pm)_{old}|}. \qquad (2.16)$$

The determinant $(detO^+)_{new}$ differs from $(detO^+)_{old}$ through the flipped Ising spin.

In the expressions above the absolute value is taken since the fermionic determinants have no definite sign. Accordingly, the average for a certain quantity A is given by

$$\begin{aligned} < A > &= \frac{\displaystyle\sum_{\{\sigma_{m,l}\}} A\, sign(detO^+ detO^-)|detO^+ detO^-|}{\displaystyle\sum_{\{\sigma_{m,l}\}} sign(detO^+ detO^-)|detO^+ detO^-|} \\ &= \frac{< A sign >_a}{< sign >_a}. \end{aligned} \qquad (2.17)$$

Here the index a denotes an average that is carried out using the absolute value of the fermionic determinants as probability distribution. If the average sign ($< sign >$) in the denominator of Eq. (2.17) is small, large fluctuations will completely deteriorate

the measurements and will cause the so-called 'minus-sign' problem[22]. Depending on the doping concentration, $< sign >$ decays exponentially with the inverse temperature and with the lattice size. We will give some results concerning the average sign later on.

The algorithm described above delivers only reliable results for $\beta \leq 4/t$. For lower temperatures (larger β or L) rounding off errors seriously affect the accuracy with which the product $B_L^\pm B_{L-1}^\pm \ldots B_1^\pm$ can be calculated since very large and very small numbers are spread all over the matrix. This problem can be overcome by using matrix factorization methods for instance the Gram-Schmidt orthogonalization procedure. The product $B_L^\pm B_{L-1}^\pm \ldots B_1^\pm$ is splitted in a product of L/k terms, which themselves are numerical accurate, because we choose k small enough. Each term can be factorized as follows[13]:

$$B_{n+k-1}^\pm \ldots B_n^\pm = U^\pm S^\pm R^\pm. \qquad (2.18)$$

$U^\pm$ is an orthogonal matrix, $S^\pm$ a diagonal one and $R^\pm$ an upper triangular matrix. The diagonal matrix, which incorporates elements with large variations in their magnitude, is easy to handle under numerical operations (especially under inversion). The practice shows that the matrix $R^\pm$ is well conditioned, whereas $U^\pm$ is well conditioned since it is orthogonal.

In the zero temperature formalism the ground state is projected out of a trial wavefunction according to[23]

$$\lim_{\Theta \to \infty} e^{-\Theta H} |\Psi_T\rangle \to |\Psi_0\rangle , \qquad (2.19)$$

where Θ is the projection parameter. In most cases we used either a Hartree-Fock trial wavefunction corresponding to the antiferromagnetic broken symmetry state or a free Fermi sea.

Since many technical details are similar in the grand canonical and in the canonical T=0 technique, we do not give a description of the projector technique.

Next we present some results concerning the average sign of the determinants obtained with the projector method. The results of the following two figures were obtained using a free Fermi sea as trial wavefunction. We performed simulations for a system of 4×4 unit cells and a set of parameters $U_d = 6$ and $\Delta = 4$ as a function of both the projection parameter Θ and the doping concentration δ.

Figure 2 shows the logarithm of the average sign as a function of the projection parameter Θ. As already pointed out above, $< sign >$ decays exponentially for larger values of Θ. This behavior is the same as in the grand canonical case.

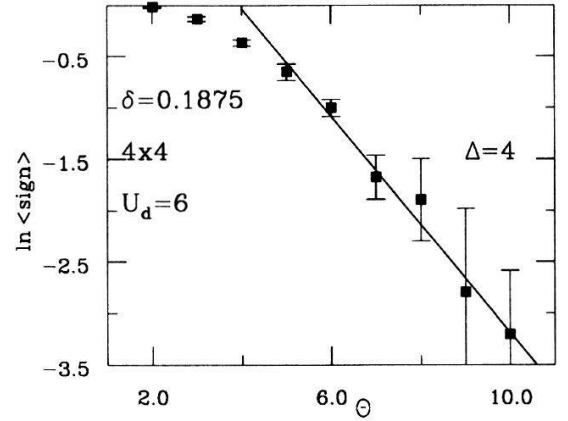Figure 3 shows the behavior of the average sign as a function of doping. We can clearly see that

Figure 2: Logarithm of the average sign as a function of the projection parameter Θ.
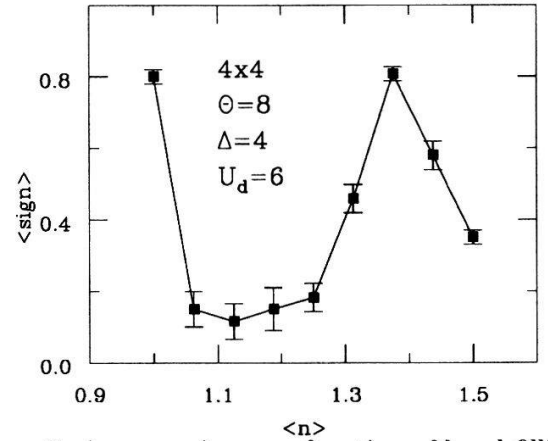

Figure 3: Average sign as a function of band filling.

a minimum develops around a doping concentration of $\delta \sim 5 - 25\%$. This point is crucial, since superconductivity is most likely to appear in this doping regime. Since $< sign >$ vanishes exponentially with Θ, ground state properties are difficult to extract in this case. The large value of $< sign >$ at $\delta = 0.375$ corresponds to a "closed shell" configuration.

The computational effort in the grand canonical finite temperature approach scales for large inverse temperatures β as $\bar{N}^3 L^2$, where $\bar{N}$ is the number of lattice sites (3 sites per unit cell in our case) and L is defined through the relation $\beta = L\Delta\tau$. $\Delta\tau$ is a small imaginary time step which we chose $\Delta\tau = 0.125$ throughout all the simulations described here.

In the canonical $T = 0$ projector method the computer time scales as $(N_\uparrow^3 + N_\downarrow^3)L$, where $N_\uparrow (N_\downarrow)$ is the number of particles with spin up (down) in the system. Since the number of holes in the three-band case (there is only one hole per unit cell) is low compared with the number of lattice sites, the projector method is in some cases more advantageous, especially in the case of large projection parameters or inverse temperatures, since it scales linearly with L.

The advantage of the grand canonical method is that it allows the calculation of thermodynamics as well as the evaluation of dynamical properties of the system.

In the last part of this section, we discuss the extraction of dynamical information from Quantum-Monte-Carlo simulations. Exact diagonalization methods are the natural framework for the calculation of dynamical properties. However serious limitations are imposed on the system size. In particular, for a realistic model like the one discussed here, the largest size is 2×2 elementary cells (12 sites). This limitation is removed by using the grand canonical QMC approach complemented by a least-squares fit[24] in order to extract the dynamical information in the system. The QMC data are given on the imaginary time axis. To obtain real frequency data, we have to perform an analytic continuation. The Matsubara thermodynamic Green's function is defined as

$$G_m(k,\tau) = \langle c_m(k,\tau)c_m^\dagger(k,0) \rangle, \qquad (2.20)$$

where the index m corresponds either to the $d_{x^2-y^2}$- or the $p_{x,y}$-orbitals. To calculate the spectral density, we have to invert the spectral representation of the Green's function

$$G_m(k,\tau) = \int_{-\infty}^{\infty} d\omega A_m(k,\omega) \frac{e^{-\tau\omega}}{1 + e^{-\beta\omega}}. \qquad (2.21)$$

This is essentially a Laplace transform, which is numerically extremely ill posed, if the data are noisy. In order to deal with this problem recent progress was made. We follow closely the approach of White et al.[24], using a modified least-squares fit.

The spectral density is defined as

$$A_m(k,\omega) = \frac{1}{Z} \sum_m \sum_{n,n'} e^{-\beta E_n}(1 + e^{-\beta(E_{n'}-E_n)})$$
$$|\langle n|c_m(k)|n'\rangle|^2 \delta(\omega - (E_{n'} - E_n)). \qquad (2.22)$$

A discretization of Eq. (2.21) yields an approximate form for the Green's function and for the spectral density, namely:

$$\bar{G}_m(k,\tau) = \sum_i \frac{a_i e^{-\tau\omega_i}}{(1 + e^{-\beta\omega_i})}, \qquad (2.23)$$

$$\bar{A}_m(k,\omega) = \sum_i a_i \delta(\omega - \omega_i). \qquad (2.24)$$

Using a least-squares fitting procedure, we can calculate the a_i's. Performing the analytic continuation, one tends to loose information in the high-energy part of the spectrum. This behavior is caused by the analytical form of the kernel in Eq. (2.21). The
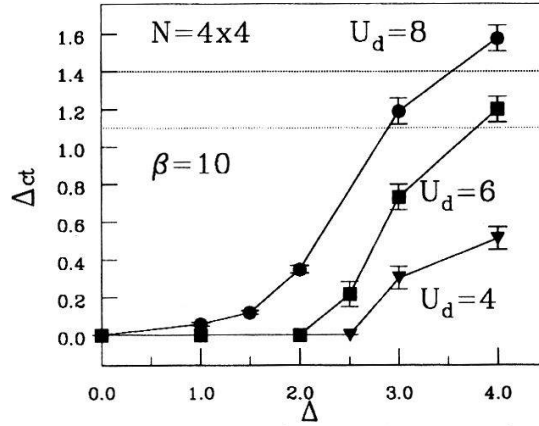

Figure 4: Charge transfer gap Δ_{CT} as a function of the charge transfer energy Δ for different values of U_d.

high-frequency parts are exponentially suppressed in $G_m(k,\tau)$. Therefore, this information can hardly be extracted out of the Monte Carlo data. However, this point is not very crucial for our purposes, since we are only interested in low-lying excitations.

III.   Normal State Properties

We will give now a direct comparison of the charge transfer gap (CTG) from Quantum-Monte-Carlo simulations and experiments for the three-band Hubbard model. The required values of the different parameters of the model for a quantitative agreement with the experimental value of the CTG are then used for the calculation of the normal state properties as well as for the superconducting properties of the model.

The region where the system is an insulator is characterized by a vanishing electronic compressibility

$$\kappa = \frac{1}{\langle n \rangle^2} \frac{\partial n}{\partial \mu}. \qquad (3.25)$$

Here we consider the total density in the elementary cell. It was previously[25] shown that (inverse) temperatures of the order of $\beta \sim 10$ are low enough in order to reach a sharp characterization of the insulating state. The width of the region with $\kappa = 0$ in terms of the chemical potential μ is taken as the CTG in the system. Figure 4 shows the CTG for several values of the parameters U_d and Δ.

The region between the two dotted horizontal lines corresponds to the experimental values[26]. It is clearly seen that only large enough values of both parameters are able to reach the region of experimental relevance. The values obtained for the CTG remain unchanged upon switching on U_p. This is due to the small double occupancy on the O-sites. This remains

true for the doping concentrations considered in this paper. Therefore we discuss in the following only the case $U_p = 0$. The influence of the parameters U_{pd} and t_{O-O} on the size of the charge-transfer gap is different. Whereas U_{pd} leads to an increase of the CTG for given values of U_d and Δ, t_{O-O} has the opposite effect. In fact, using values suggested by several authors[1-7] for both parameters, the changes in the CTG cancel each other. The same happens for other properties and in the cases discussed in the following we omit these parameters. This may seem a drastic approximation since the operator corresponding to U_{pd} was proposed as a possible candidate to obtain pair-attraction which could lead to superconductivity (or phase separation) in the system. We checked both with Monte Carlo simulations and exact diagonalization that in order to obtain sizable effects due to this operator, rather large values of U_{pd} ($\gtrsim 2$) are necessary. For the range of values proposed in Refs. 1-7, the direct O-O hopping cancels the effect of U_{pd}. For definiteness we will consider in the following $U_d = 6$ and $\Delta = 4$. The parameters chosen above lead to a value of the local magnetic moment of $< s_z^2 > \sim 0.84$ that implies that approximately 90% of the moment corresponding to a spin-$\frac{1}{2}$ is localized on the Cu-site. This value is almost not changed as a function of doping reaching $< s_z^2 > \sim 0.78$ at 50% doping[25]. This result agrees with neutron scattering experiments[27], where no dependence on doping was found in the integrated intensity. Unfortunately no value for the local magnetic moment can be extracted from those experiments. The Monte Carlo results show that doping does not lead to large charge fluctuations on the Cu site and the fact that a well developed magnetic moment remains, lends support to models where spin fluctuations play a central role also in the doped region.

The most salient characteristics of the high-T_c superconductors besides the superconductivity itself are the magnetic properties. In the absence of doping, the HTS are insulators with antiferromagnetic long-range order[28] as a result of electronic correlation.

To decide whether the three-band Hubbard model also exhibits antiferromagnetic long-range order, we performed finite size studies with system sizes up to 10×10 unit cells with three sites each and inverse temperatures (projection parameters) up to $\beta = 30$ ($\Theta = 80$).

Figure 5 shows a comparison of the magnetic structure form factor on the Cu-sites at the wavevector $\vec{k} = (\pi, \pi)$ obtained with both QMC methods. The magnetic structure form factor is given by

$$S(\vec{k}) = \sum_{\vec{\ell}} e^{i\vec{k} \cdot \vec{\ell}} C(\ell_x, \ell_y), \qquad (3.26)$$

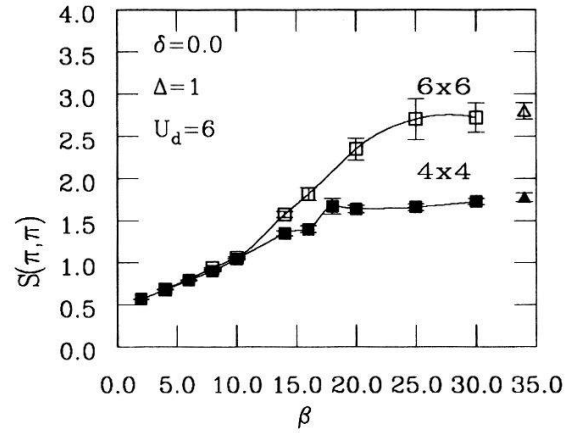
Figure 5: $S(\pi, \pi)$ as function of the inverse temperature β.

where

$$C(\ell_x, \ell_y) = \frac{1}{N} \sum_i \langle (n_{i\uparrow}^d - n_{i\downarrow}^d)(n_{i+\ell\uparrow}^d - n_{i+\ell\downarrow}^d) \rangle \quad (3.27)$$

is the spin-spin correlation function. We evaluate the magnetic properties only on the Cu-sites. Analogous to results obtained for the one-band model, $S(\vec{k})$ exhibits a sharp peak at the wavevector $\vec{k} = (\pi, \pi)$. Full and open squares mark results obtained with the grand canonical method for system sizes of 4×4 and 6×6 unit cells respectively, whereas full and open triangles correspond to results of the projector method. The data obtained with both techniques coincide within the error bars. As can be seen from Figure 5, the inverse temperature needed to reach the ground state with the finite temperature approach is approximately $\beta \simeq 20 - 25$ compared to $\beta \simeq 10$ in one-band calculations[14, 22]. This can be understood by considering that the bandwidth of the lowest band for the noninteracting system (which is half-filled in the undoped case) is given by

$$W = \sqrt{\left(\frac{\Delta}{2}\right)^2 + 8} - \frac{\Delta}{2} \qquad (3.28)$$

in units of the copper-oxygen hybridization t_{Cu-O}, compared to $W = 8t$ in the one-band Hubbard model. As can be seen from Eq. (3.28) the temperatures required to reach the ground state at large values of Δ decreases since the bandwidth decreases as well. The simulations for $T = 0$ were performed with projection parameters $\Theta = 40 - 80$.

Figure 6 shows an extrapolation of $S(\pi, \pi)$ vs. the linear system size (in units of the lattice constants) for $U_d = 6$ and the charge-transfer energies $\Delta = 4$ and $\Delta = 1$. These calculations were done with the projector method. The case $\Delta = 4$ that – as discussed above – gives a charge transfer gap
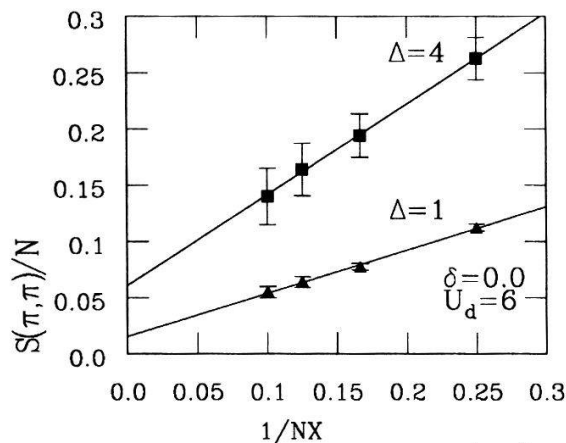
Figure 6: Finite size scaling of $S(\pi, \pi)$.

of $\Delta_{ct} \simeq 1.2t_{pd}$ ($\simeq 1.7$ eV) in quantitative agreement with experiments, leads to a staggered magnetization of $m = \sqrt{3m_z^2} = 0.42 \pm 0.11$, whereas we find for $\Delta = 1$ a value of $m = 0.22 \pm 0.04$. Since the parameter set with $\Delta = 4$ leads to an agreement with experiments for several quantities, as remarked above, it is interesting to compare the values obtained for the order parameter with the corresponding ones in the S-$\frac{1}{2}$ antiferromagnetic Heisenberg model and in the one-band Hubbard model. For the first one, $m = 0.60 \pm 0.04$[29], showing that fluctuations are stronger in the three-band model. On the other hand, a similar value of the staggered magnetization can be obtained in the one-band Hubbard model only with relatively large coupling constants $(U \gtrsim 6-8)$[14]. Therefore, if an identification of both models is to be made, this is possible only in the strong coupling regime of the one-band Hubbard model. Figure 6 also shows that both the weak and strong-coupling case scale as $1/\sqrt{N}$, implying that fluctuations are well described by spin-wave theory[30].

We consider finally the consequences of doping for the magnetic properties. Figure 7 shows the magnetic structure form factor both for $\Delta = 4$ (Figure 7a) and $\Delta = 1$ (Figure 7b) for a doping concentration of $\delta = 0.22$. Analogous to the behavior in the one-band model[15] there is a shift of the maximum of $S(\vec{k})$ along the (1,0) line in reciprocal space. It seems therefore to be a generic behavior of doped correlated systems. The incommensurate structure is short ranged as comparisons of calculations for different lattice sizes have shown. However, such a structure is only observed in $La_{2-x}Sr_xCuO_4$[31] but not until now in $YBa_2Cu_3O_{7-y}$. This indicates that some factors extrinsic to the CuO_2 planes are responsible for the not observation of an incommensurable structure in $YBa_2Cu_3O_{7-y}$.

Another magnetic quantity we consider is the
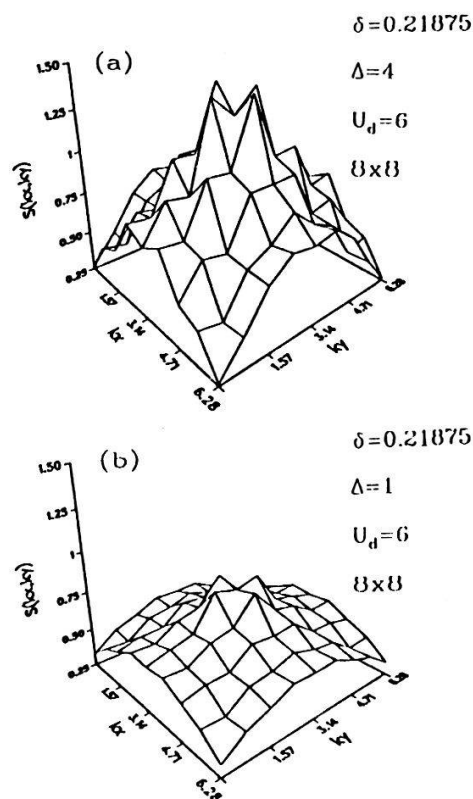
Figure 7: Magnetic structure factor for a doping concentration of $\delta = 0.21875$ (a): $\Delta = 4$ and (b): $\Delta = 1$.

magnetic susceptibility

$$\chi(\vec{k} = 0) = \frac{1}{N} \sum_{i,i'} \int_0^\beta d\tau < (n_{i\uparrow}^d(\tau) - n_{i\downarrow}^d(\tau))$$
$$(n_{i'\uparrow}^d(0) - n_{i'\downarrow}^d(0)) > \qquad (3.29)$$

as a function of doping for different values of the parameter Δ that range from a situation, where large charge fluctuations take place on the Cu-site $(\Delta \sim 1)$, to a situation where a well developed spin-moment is present at that site $(\Delta \sim 4)$.

Figure 8 shows that only large values of Δ are able to lead to a maximum at finite doping that appears in experiments[9]. In the case $\Delta = 1$, $\chi(\vec{k} = 0)$ is a monotonically decreasing function for $\delta > 0$, a behavior that qualitatively differs from experiments. It is interesting to notice that a maximum was also obtained by Trugman in the $t-t'-J$ model for values of the Hubbard interaction $U/t \gtrsim 8$[12]. Moreover it appears in the one-band Hubbard model in the frame of a slave boson approximation only if sufficiently large values of U $(\gtrsim 6 - 8)$ are used[32]. The maximum in the magnetic susceptibility as a function of doping seems therefore to be a characteristic of strongly correlated systems, a feature that apparently was not appreciated enough until now.
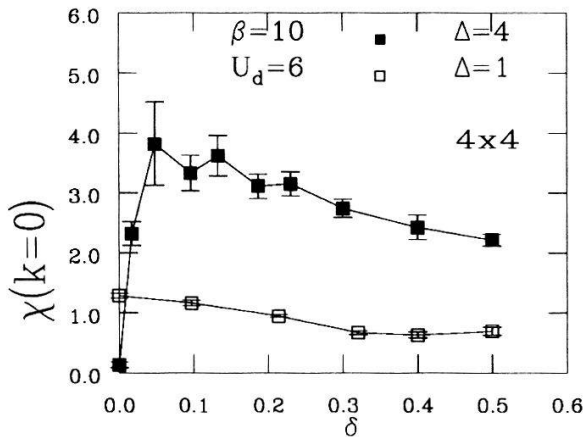
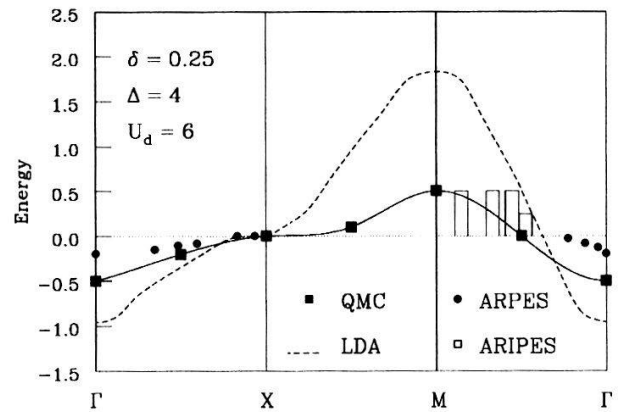Figure 8: Magnetic susceptibility as a function of doping.

Figure 9: Dispersion of the Zhang-Rice states in the irreducible part of the Brillouin zone. The dashed line gives the LDA-bandstructure. The experiments are also depicted in the figure.

We turn now to the dynamical properties for one-particle excitations. A central and controversial issue in the high-T_c cuprates concerns the nature of carriers near the Fermi surface. The most crucial experimental results until now stem from angle-resolved photoemission (ARPES) and inverse photoemission (ARIPES)[33, 34] measurements that clearly show the existence of a dispersive band that crosses the Fermi surface. The topology of the Fermi surface is in general agreement with LDA-bandstructure calculations[35, 36], however the Fermi velocity is quite different. This indicates that electronic correlations renormalize considerably the results obtained in the frame of a one-particle treatment. So far, strong correlation effects can be properly taken into account only by exact numerical methods. Data concerning the dynamics of charge carriers near the Fermi surface are available up to now only in the context of the $t - J$ model with exact diagonalization[37-41].

In the grand canonical Quantum-Monte-Carlo method we can calculate the Matsubara thermodynamic Green's function. In order to evaluate the spectral density we have to perform an analytic continuation. We used a modified least-squares fit[24] to obtain the spectral density $A(\vec{k}, \omega)$. The results of the least-squares fitting procedure are most reliable for small excitation energies. For each $\vec{k}$-vector we extracted the energy of the state closest to the Fermi energy. These states have both copper and oxygen weight and are mainly of Zhang-Rice character[42].

In Figure 9 we show results for a lattice of 4×4 unit cells and for the above defined parameter set. The doping is $\delta = 0.25$ and the inverse temperature is $\beta = 10$. We see that concerning the Fermi surface and the Fermi velocity the dispersion of the Zhang-Rice states is in very good agreement with ARPES and ARIPES experimental data which were measured in $Bi_2Sr_2CaCu_2O_8$[33] at a doping concentration of about

20%[43]. This result shows that the three-band Hubbard model describes accurately the one-particle excitations of the superconducting oxides. The LDA bandstructure (dashed line) totally overestimates the Fermi velocity although the locus of the Fermi energy is given correctly[35]. On the other hand, as already pointed out above, the parameter set ($\Delta = 4, U_d = 6$) has been confirmed as a good starting point in order to investigate the superconducting behavior in these systems.

Using a exact diagonalization study for a 2×2 system we address the question whether the present system can be well described by a Fermi liquid picture (Figure 10). For a doping concentration of 50 % the imaginary part of the self-energy ($\mathrm{Im}\,\Sigma(k, \omega)$) vanishes for $\vec{k} = (\pi, 0)$ in a broad region around the Fermi energy. This clearly indicates the existence of long-living quasiparticles and the Fermi liquid picture is appropriate. However, for a doping of $\delta = 0.25$, $\mathrm{Im}\,\Sigma(k, \omega)$ does not vanish on approaching the Fermi energy. Therefore, the corresponding Zhang-Rice state has a finite lifetime in the immediate vicinity of E_F and the Fermi liquid picture with well defined quasiparticles at the Fermi energy breaks down. We suggest that at doping levels $\delta \lesssim 0.25$, which are relevant for the high-T_c cuprates, the system is better described as a Luttinger liquid.

IV.   Superconducting Properties

Next we discuss the interaction vertex of pairing correlation functions for the extended s-wave symmetry of the order parameter. The interaction vertex[16, 44] is defined as the difference between the equal time
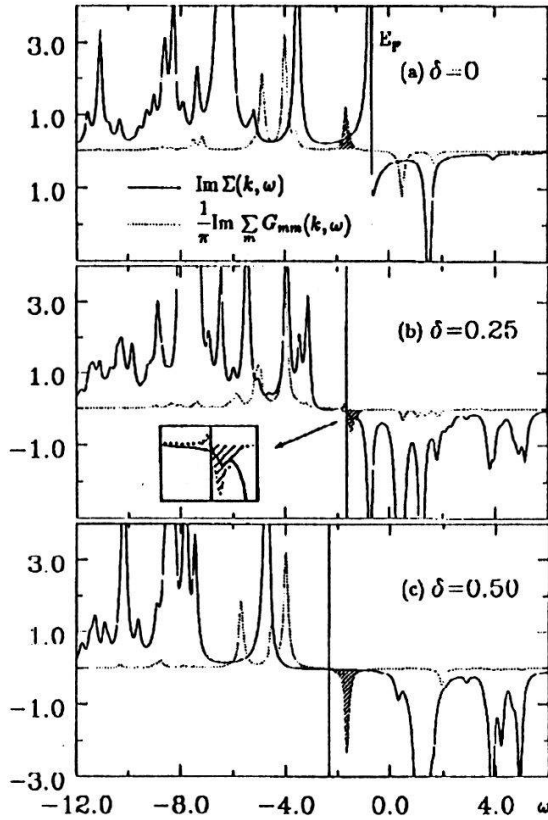
Figure 10: Imaginary part of the self-energy at $\vec{k} = (\pi, 0)$.

Figure 11: Extended s-wave vertex as a function of doping.

pairing correlation function (P_α)

$$P_\alpha = \langle \Delta_\alpha \Delta_\alpha^\dagger \rangle , \qquad (4.30)$$

where $\Delta_\alpha^\dagger$ denotes a pair-field operator, and the corresponding quantity for two fully dressed one-particle excitations that propagate without interaction $(\bar{P}_\alpha)$. A positive interaction vertex means that the interaction enhances pairing. We have considered different symmetry channels. For an explicit definition of the underlying operators Δ_α see Ref. 24.

Figure 11 shows the dependence of the vertex for extended s-wave symmetry of the order parameter as a function of doping. As mentioned before we take into account only those contribution for two holes separated by one lattice constant both on the Cu- and on the O-sublattices. The (inverse) temperature of the simulation is $\beta = 10$, the lowest temperature attainable without running into minus sign problems. It can be seen that a distinct maximum appears for a doping of $\delta \sim 20\%$ and the overall shape of the curve is very reminiscent of the corresponding experimental curve for T_c in $La_{2-x}Sr_xCuO_4$[8, 9]. On the contrary, in the case of d-wave symmetry, the maximum is always found at zero doping. In contrast to the presently studied three-band model, the results by Moreo and Scalapino[16] for the one-band Hubbard
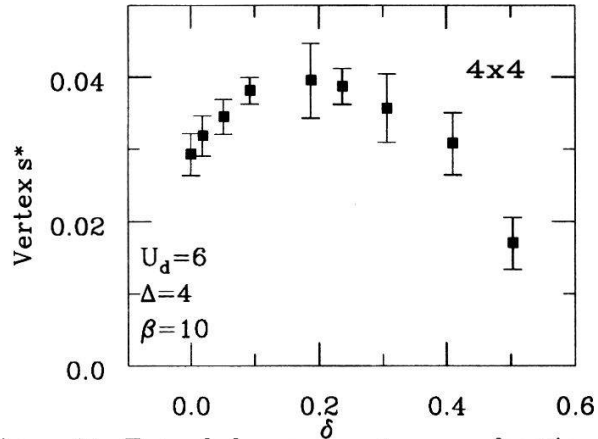
model do not show such a marked variation of the vertex as a function of doping. For other parameter regions $(\Delta \sim 1)$, where charge fluctuations dominate over spin fluctuations, again the maximum is obtained for zero doping but now for both s- and d-wave symmetry. We have also examined the case of nodeless s-wave, i.e. pairs formed either on-site on both Cu or O or such pairs that are separated by half a lattice constant (in x-, y- or both directions). With and without $U_{pd} = 0.5$ the vertex remained negative or zero within error bars for all doping concentrations. Therefore, for the values of U_{pd} consistent with parameter determinations in the literature[1–7], it is seen that the corresponding operator does not play any role for superconductivity.

Since the simulations were performed at finite temperatures, long-range order is not going to set in as a consequence of the Mermin-Wagner theorem[45]. But one could expect that the system undergoes a Kosterlitz-Thouless phase transition at a certain finite temperature as in the negative-U Hubbard model[46]. We have simulated systems with 4×4, 6×6 and 8×8 elementary cells with 3 atoms each. No measurable change was detected for the different sizes. However, contrary to the one-band case, where the pairing function levels off at around $\beta \sim 6$, the results for the three-band model seem to have not yet reached convergence in temperature (Figure 12).

Again the results differ in the parameter region $\Delta \sim 1$, where already at $\beta \sim 8$ a convergent behavior is observed. Thus although off-diagonal (quasi) long-range order is not obtained in our simulations, Figure 12 shows that the relevant temperature scale for superconductivity was still not reached for the extended s-channel with the parameter set used in the present model. This fact together with Figure 11 implies that the three-band model remains a serious candidate for superconductivity induced by electron-
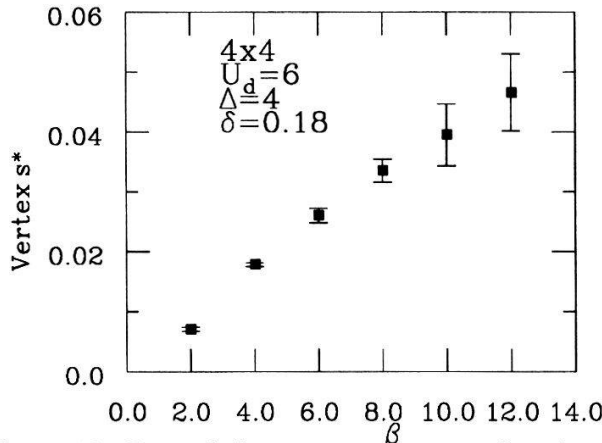
Figure 12: Extended s-wave vertex as a function of the inverse temperature.

ic correlation in contrast to the one-band Hubbard model, where numerical results failed up to now to show any evidence for superconductivity in the experimentally relevant symmetry channel of the order parameter.

V.   Summary

In summary we have determined a parameter set for the three-band Hubbard model that leads to a quantitative agreement with experimental results for the CTG.

In the undoped case antiferromagnetic long-range order is found both in the weak ($U_d = 6, \Delta = 1$) and strong ($U_d = 6, \Delta = 4$) coupling situations. The structure form factor scales in both regions as $1/\sqrt{N}$, where N is the number of Cu-sites in the system. Fluctuations are therefore well described by spin-wave theory. In the physically relevant case ($U_d = 6, \Delta = 4$), the extrapolated value for the staggered magnetization corresponds to a fairly strong coupling situation in the one-band Hubbard model ($U \gtrsim 6 - 8$). Doping leads to incommensurate short ranged magnetic structures both in the weak and in the strong coupling case, as it was also observed in the one-band Hubbard model. The presence of this structure seems therefore to be a generic property of such correlated systems. We suggest that the fact that it is not observed in $YBa_2Cu_3O_{7-y}$, in contrast to $La_{2-x}Sr_xCuO_4$, is due to factors extrinsic to the CuO_2 planes. Finally it should be noticed that the magnetic properties considered here do not lead to qualitative but only quantitative differences between the weak and strong coupling cases. This is in contrast to the behavior of the magnetic susceptibility, where we find only in the $\Delta = 4$ realistic regime of the parameter space a behavior that is qualitatively

the same than in experiments. Moreover, our numerical results show that the three-band Hubbard model gives a very accurate description of the low-lying one-particle excitations in the high-T_c superconductors. We can reproduce the experimentally observed Fermi surface and Fermi velocity quantitatively. Finally, the same parameter set gives an interaction vertex in the extended s-channel of the pairing functions, where the doping dependence suggestively resembles the one of T_c as found in experiments. The features above are not obtained in other parameter regions.

References

[1] A. K. McMahan, J. F. Annett, and R. M. Martin, *Phys. Rev. B* **42** (1988) 6268, *and references therein.*

[2] J. B. Grant and A. K. McMahan, *Phys. Rev. Lett* **66** (1991) 488.

[3] A. K. McMahan, R. M. Martin, and S. Satpathy, *Phys. Rev. B* **39** (1988) 6650.

[4] H. Eskes and G. A. Sawatzky, *Phys. Rev. Lett* **61** (1988) 1415.

[5] F. Mila, *Phys. Rev. B* **38** (1988) 11358.

[6] H. Eskes, L. H. Tjeng, and G. A. Sawatzky *Phys. Rev. B* **41** (1990) 288.

[7] Y. Ohta, T. Tohyama, and S. Maekawa, *Phys. Rev. Lett* **66** (1991) 1228.

[8] J. B. Torrance, *et al*, *Phys. Rev. Lett* **61** (1988) 1127.

[9] J. B. Torrance, *et al*, *Phys. Rev. B* **40** (1989) 8872.

[10] H. Takagi, *et al*, *Phys. Rev. B* **40** (1989) 2254.

[11] J. R. Cooper, *et al*, *Phys. Rev. B* **35** (1987) 8794.

[12] S. A. Trugman, *Phys. Rev. Lett* **65** (1990) 500.

[13] S. R. White, *et al*, *Phys. Rev. B* **40** (1989) 506.

[14] J. E. Hirsch and S. Tang, *Phys. Rev. Lett* **62** (1989) 591.

15 A. Moreo *et al*, *Phys. Rev. B* **41** (1989) 2313.

16 A. Moreo and D. J. Scalapino, *Phys. Rev. B* **43** (1991) 8211.

17 F. C. Zhang and T.M. Rice, *Phys. Rev. B* **37** (1988) 3759.

18 R. Blankenbecler, D. J. Scalapino, and R. L. Sugar, *Phys. Rev. D* **24** (1981) 2278.

19 J. E. Hirsch, *Phys. Rev. B* **31** (1985) 4403.

20 J. E. Hirsch, *Phys. Rev. B* **28** (1983) 4059.

21 J. P. Kogut, *Rev. Mod. Phys* **55** (1983) 775.

22 E. Y. Loh, J.E. Gubernatis, R.T. Scalettar, S.R. White, D.J. Scalapino, and R.L. Sugar, *Phys. Rev. B* **41** (1990) 9301.

23 S. Sorella, *et al*, *Int. J. Mod. Phys. B* **1** (1988) 993; S. Sorella, S. Baroni, R. Car, and M. Parrinello, *Europhys. Lett* **8** (1989) 663.

24 S. R. White, *et al*, *Phys. Rev. Lett* **63** (1989) 1523.

25 G. Dopf, A. Muramatsu, and W. Hanke, *Phys. Rev. B* **41** (1990) 9264.

26 H. Romberg, *et al*, *Z. Phys. B* **78** (1990) 367; Y. Ohta, *et al*, *Phys. Rev. Lett* **66** (1991) 1228, *and references therein.*

27 R. J. Birgeneau, *et al*, *Phys. Rev. B* **38** (1988) 6614.

28 Y. Endoh, *et al*, *Phys. Rev. B* **37** (1988) 7443; J. M. Tranquada, *et al*, *Phys. Rev. Lett* **60** (1988) 156.

29 J. D. Reger and A. P. Young, *Phys. Rev. B* **37** (1988) 5978.

30 D. A. Huse, *Phys. Rev. B* **37** (1988) 2380.

31 T. R. Thurston, *et al*, *Phys. Rev. B* **40** (1989) 4585.

32 L. Lilly, A. Muramatsu, and W. Hanke, *to be published.*

33 G. Mante, *et al*, *Z. Phys. B* **80** (1990) 181.

34 C. G. Olson, *et al*, *Phys. Rev. B* **42** (1990) 381; T. Takahashi, *et al*, *Phys. Rev. B* **39** (1989) 6636.

35 M. S. Hybertsen and L. F. Mattheiss, *Phys. Rev. Lett* **60** (1988) 1161.

36 H. Krakauer and W. E. Pickett, *Phys. Rev. Lett* **60** (1988) 1165.

37 K. J. von Szczepanski, P. Horsch, W. Stephan, and M. Ziegler, *Phys. Rev. B* **41** (1990) 2017.

38 E. Dagotto, *et al*, *Phys. Rev. B* **41** (1990) 9049.

39 Y. Hasegawa and D. Poilblanc, *Phys. Rev. B* **41** (1990) 9555.

40 D. Poilblanc and E. Dagotto, *Phys. Rev. B* **42** (1990) 4861.

41 W. Stephan and P. Horsch, *Phys. Rev. Lett* **66** (1991) 2258.

42 J. Wagner, W. Hanke, and D.J. Scalapino, *Phys. Rev. B* **43** (1991) 10517.

43 W. A. Groen, *et al*, *Physica C* **165** (1990) 55.

44 S. R. White, *et al*, *Phys. Rev. B* **39** (1989) 839.

45 N. D. Mermin and H. Wagner, *Phys. Rev. Lett* **17** (1966) 1133.

46 A. Moreo and D. J. Scalapino, *Phys. Rev. Lett* **66** (1991) 946.